Dynamic Characteristics Analysis of Multilayer Fiber Reinforced Plastic Shaft

QIAN Haiyu, *ZHU Junchao**, *WEN Huabing*, *HE Congshuai*

School of Energy and Power Engineering, Jiangsu University of Science and Technology, Zhenjiang 212100, P. R. China

(Received 10 January 2022; revised 12 February 2022; accepted 15 February 2022)

Abstract: In order to study the dynamic characteristics of multilayer fiber reinforced plastic (MFRP) shaft, the coupling model of three-dimensional equivalent bending stiffness theory and transfer matrix method is established, and the influence of thickness-radius ratio, length-radius ratio, layer angles, layer proportion, and stacked approaches on MFRP shaft dynamic characteristics is investigated. The result shows that the proposed coupling model has high accuracy in MFRP shaft dynamic performance prediction. The proportion of small-angle layers is the decisive factor of MFRP shaft natural frequency. With the increase of thickness-radius ratio and length-radius ratio, the natural frequency of MFRP shaft decreases. The natural frequency of MFRP shaft with the angle layers combination of ±45° and ±90° is smaller compared with the metal shaft no matter in simple/free boundary condition or simple/simple supported boundary condition.

Key words: multilayer fiber reinforced plastic (MFRP) shaft; dynamic characteristics; natural frequency

CLC number: TH133;TB332 **Document code:** A **Article ID:** 1005-1120(2022)01-0087-11

0 Introduction

In recent years, multilayer fiber reinforced plastic(MFRP) shaft has been widely used in mechanical arm, drive shaft, electrical conduit, satellite truss structures, and unmanned aerial vehicle system (UAVs)[1]. Compared with the traditional metal shaft, the MFRP shaft has the characteristics of light weight, high specific strength, and high specific modulus[2-3], which can improve its natural frequency and effectively reduce vibration and noise. In addition, stacking parameters of MFRP shaft can be changed, such as layer angles, number of layers, stacked approaches, discrete layer thickness, etc[4-5], so the corresponding dynamic design can be carried out according to different requirements.

The stacking parameters of MFRP shaft have been deeply studied by domestic and foreign scholars. For layer angles, Badie et al.[6] investigated the effect of layer angles on the natural frequency of MFRP shaft. It shows that the natural frequency of MFRP shaft increases as the layer angles decrease and MFRP shaft containing ±45° angle layers has a high load-carrying capacity and torsion stiffness. Menshykova et al.[7] found that the MFRP shaft with 0° angle layers has a high ability to bear bending load, while the MFRP shaft with 90° angle layers has negligible improvement in bending resistance. Sun et al.[8] analyzed the natural frequency of carbon fiber reinforced plastic(CFRP) shaft embedded in metal flange by using finite element method, and further proposed that the effect of layer angles on the natural frequency of CFRP shaft is greater than layers thickness. In terms of the stacking sequence, Gubran and Gupta[9] analyzed and optimized the dynamic stresses in composite shafts by using modified equivalent modulus beam theory, investigated the effect of stacking sequence on the natural frequency of composite shafts, and verified the accuracy of the model.

Also, several relevant dynamical modeling theories have been proposed. Gubran[10] proposed an

---

*Corresponding author, E-mail address: zjc330@126.com.

How to cite this article: QIAN Haiyu, ZHU Junchao, WEN Huabing, et al. Dynamic characteristics analysis of multilayer fiber reinforced plastic shaft[J]. Transactions of Nanjing University of Aeronautics and Astronautics, 2022, 39(1): 87-97.

http://dx.doi.org/10.16356/j.1005-1120.2022.01.009

equivalent modulus beam theory that took into account the stacking sequence. Sino et al.[11] further proposed a simplified homogeneous beam theory utilizing stacking sequence and fiber orientation. Subsequently, Sevkat and Saeed et al.[12-13] investigated the influence of composite stacking parameters on the shaft natural frequency by means of homogeneous beam theory. To overcome the limitation that homogeneous beam theory can only solve for the equivalent bending stiffness of composite shafts with symmetrical laminated structure, Montagnier et al.[14] proposed a design for composite shafts based on a simply supported beam model, which can be used to study the dynamics of laminated structural shafts with non-symmetrical layers. Khoshravan et al.[15] designed the composite shaft based on classical laminated theory and carried out modal simulations by using ANSYS. Ding et al.[16] analyzed the natural frequency of the composite shaft with the finite element method(FEM), and verified the feasibility of FEM. Ren et al.[17] analyzed the effects of layer angles, rotation speed, and length-radius ratio on the natural frequency of CFRP transmission shaft based on the theory of composite thin-walled beam with the variational asymptotic method. Ding et al.[18] designed a lay-up scheme for CFRP drive shafts based on automotive drive shafts and verified the accuracy of the transfer matrix method.

In summary, equivalent modulus beam theory, classical lamination theory, three-dimensional analytical model, and finite element method are used to analyze the dynamics characteristics of CFRP shaft. For equivalent modulus beam theory, it does not reflect the effect of stacking sequence. The classical lamination theory applies to the thin-walled condition. Three-dimensional analytical model and finite element method can be used to solve the dynamics problem of the CFRP shaft. However, once the model is complicated, both of the two methods are time-consuming. In this paper, the coupling model which combines equivalent bending stiffness theory and transfer matrix method is proposed to analyze the dynamics characteristics of MFRP shaft. The equivalent bending stiffness theory is established based on three-dimensional analytical model. Moreover, there are few studies on MFRP shaft considering the effect of thickness-radius ratio, length-radius ratio, stacked approaches, and boundary conditions. Therefore, this paper studies the influence of layer angles, layer proportion and stacked approaches on the natural frequency of MFRP shafts under different thickness-radius ratios, length-radius ratios, and boundary conditions with the proposed coupling model.

1 Theoretical Equations

1.1 Equivalent bending stiffness theory based on three-dimensional analytical model

The stiffness matrix for the single-layer stress-strain relationship in a coordinate system can be obtained as[19]

$$\begin{Bmatrix}\sigma_1\\ \sigma_2\\ \sigma_3\\ \tau_{23}\\ \tau_{13}\\ \tau_{12}\end{Bmatrix}=\begin{bmatrix}Q_{11} & Q_{12} & Q_{13} & 0 & 0 & 0\\ Q_{12} & Q_{22} & Q_{23} & 0 & 0 & 0\\ Q_{13} & Q_{23} & Q_{33} & 0 & 0 & 0\\ 0 & 0 & 0 & Q_{44} & 0 & 0\\ 0 & 0 & 0 & 0 & Q_{55} & 0\\ 0 & 0 & 0 & 0 & 0 & Q_{66}\end{bmatrix}\begin{Bmatrix}\varepsilon_1\\ \varepsilon_2\\ \varepsilon_3\\ \gamma_{23}\\ \gamma_{13}\\ \gamma_{12}\end{Bmatrix} \tag{1}$$

where Q_{ij} is the coefficient of positive-axis compliance. σ_1, σ_2 and σ_3 are the normal stresses, ε_1, ε_2 and ε_3 the strain components, τ_{23}, τ_{13} and τ_{12} the shear stress components, and γ_{23}, γ_{13} and γ_{12} the engineering shear strain components.

Based on the stress-strain theory of material mechanics, the positive-axis matrix $\boldsymbol{Q}$ of a single-layer can be obtained as

$$\boldsymbol{Q}=\begin{bmatrix}1/E_1 & -\nu_{21}/E_2 & -\nu_{31}/E_3 & 0 & 0 & 0\\ -\nu_{12}/E_1 & 1/E_2 & -\nu_{32}/E_3 & 0 & 0 & 0\\ -\nu_{13}/E_1 & -\nu_{23}/E_2 & 1/E_3 & 0 & 0 & 0\\ 0 & 0 & 0 & 1/G_{23} & 0 & 0\\ 0 & 0 & 0 & 0 & 1/G_{13} & 0\\ 0 & 0 & 0 & 0 & 0 & 1/G_{12}\end{bmatrix}^{-1} \tag{2}$$

where ν_{ij} is the Poisson's ratio in the i, j direction, G_{ij} the shear modulus in the i, j direction, and E_1, E_2, E_3 are the Young's modulus.

To facilitate the calculation of the hollow shaft, the above positive-axis matrix is transformed to the off-axis and then the expression in column coordinates is obtained. At this point, the principal equation for the direction of fiber orientation at angle φ to the axial z is given as

$$\begin{Bmatrix} \sigma_z \\ \sigma_\theta \\ \sigma_r \\ \tau_{\theta r} \\ \tau_{zr} \\ \tau_{z\theta} \end{Bmatrix}_\varphi = \begin{bmatrix} \bar{Q}_{11} & \bar{Q}_{12} & \bar{Q}_{13} & 0 & 0 & \bar{Q}_{16} \\ \bar{Q}_{12} & \bar{Q}_{22} & \bar{Q}_{23} & 0 & 0 & \bar{Q}_{26} \\ \bar{Q}_{13} & \bar{Q}_{23} & \bar{Q}_{33} & 0 & 0 & \bar{Q}_{36} \\ 0 & 0 & 0 & \bar{Q}_{44} & \bar{Q}_{45} & 0 \\ 0 & 0 & 0 & \bar{Q}_{45} & \bar{Q}_{55} & 0 \\ \bar{Q}_{16} & \bar{Q}_{26} & \bar{Q}_{36} & 0 & 0 & \bar{Q}_{66} \end{bmatrix} \begin{Bmatrix} \varepsilon_z \\ \varepsilon_\theta \\ \varepsilon_r \\ \gamma_{\theta r} \\ \gamma_{zr} \\ \gamma_{z\theta} \end{Bmatrix}_\varphi \tag{3}$$

where $\bar{Q}_{ij}$ is the coefficient of off-axis compliance; r, θ and z are the radial, hoop and axial coordinates.

In the above equations, $\bar{Q}_{11}=m^4Q_{11}+2m^2n^2(Q_{12}+2Q_{66})+n^4Q_{22}$; $\bar{Q}_{33}=Q_{33}$; $\bar{Q}_{44}=m^2Q_{44}+n^2Q_{55}$; $\bar{Q}_{12}=m^2n^2(Q_{11}+Q_{22}-4Q_{66})+(m^4+n^4)Q_{12}$; $\bar{Q}_{36}=mn(Q_{13}-Q_{23})$; $\bar{Q}_{13}=m^2Q_{13}+n^2Q_{23}$; $\bar{Q}_{16}=mn[m^2(Q_{11}-Q_{12}-2Q_{66})+n^2(Q_{12}-Q_{22}+2Q_{66})]$; $\bar{Q}_{45}=mn(Q_{55}-Q_{44})$; $\bar{Q}_{55}=n^2Q_{44}+m^2Q_{55}$; $\bar{Q}_{22}=n^4Q_{11}+2m^2n^2(Q_{12}+2Q_{66})+m^4Q_{22}$; $\bar{Q}_{23}=n^2Q_{13}+m^2Q_{23}$; $Q_{22})+(n^2-m^2)^2Q_{66}$; $\bar{Q}_{26}=mn[n^2(Q_{11}-Q_{12}-2Q_{66})+m^2(Q_{12}-Q_{22}+2Q_{66})]$ ($m=\cos\varphi$, $n=\sin\varphi$).

As a reference for the general production process of composite hollow shafts, alternating $-\varphi$ and $+\varphi$ angle layers are usually stacked and the thickness of the lay-ups is kept uniform. It is assumed that the bonding layer between the individual layers is negligibly thin and the thicknesses of the layer satisfy the thin-walled assumption. Treating the $\pm\varphi$ angle layers as a minimum mechanical unit and then summing the corresponding intrinsic structure matrix, Eq.(3) can be converted as

$$\begin{Bmatrix} \sigma_z \\ \sigma_\theta \\ \sigma_r \\ \tau_{\theta r} \\ \tau_{zr} \\ \tau_{z\theta} \end{Bmatrix}_{\pm\varphi} = \begin{bmatrix} \bar{Q}_{11} & \bar{Q}_{12} & \bar{Q}_{13} & 0 & 0 & 0 \\ \bar{Q}_{12} & \bar{Q}_{22} & \bar{Q}_{23} & 0 & 0 & 0 \\ \bar{Q}_{13} & \bar{Q}_{23} & \bar{Q}_{33} & 0 & 0 & 0 \\ 0 & 0 & 0 & \bar{Q}_{44} & 0 & 0 \\ 0 & 0 & 0 & 0 & \bar{Q}_{55} & 0 \\ 0 & 0 & 0 & 0 & 0 & \bar{Q}_{66} \end{bmatrix} \begin{Bmatrix} \varepsilon_z \\ \varepsilon_\theta \\ \varepsilon_r \\ \gamma_{\theta r} \\ \gamma_{zr} \\ \gamma_{z\theta} \end{Bmatrix}_{\pm\varphi} \tag{4}$$

Notice that it is necessary to take into account the effects of stresses and strains in the cross-section when building a three-dimensional analytical model based on a thick-walled beam. The relationship between the components of the cross-sectional internal strains and external strains can be expressed as

$$\begin{cases} \varepsilon_r = A_1\varepsilon_z + A_2\gamma_{z\theta} \\ \varepsilon_\theta = A_3\varepsilon_z + A_4\gamma_{z\theta} \\ \gamma_{\theta r} = A_5\gamma_{zr} \end{cases} \tag{5}$$

where $A_1=\dfrac{\bar{Q}_{12}\bar{Q}_{23}-\bar{Q}_{22}\bar{Q}_{13}}{\bar{Q}_{22}\bar{Q}_{33}-\bar{Q}_{23}^2}$;

$A_2=\dfrac{\bar{Q}_{26}\bar{Q}_{23}-\bar{Q}_{22}\bar{Q}_{36}}{\bar{Q}_{22}\bar{Q}_{33}-\bar{Q}_{23}^2}$; $A_3=\dfrac{\bar{Q}_{13}\bar{Q}_{23}-\bar{Q}_{12}\bar{Q}_{33}}{\bar{Q}_{22}\bar{Q}_{33}-\bar{Q}_{23}^2}$;

$A_4=\dfrac{\bar{Q}_{23}\bar{Q}_{36}-\bar{Q}_{26}\bar{Q}_{33}}{\bar{Q}_{22}\bar{Q}_{33}-\bar{Q}_{23}^2}$; $A_5=\dfrac{-\bar{Q}_{45}}{\bar{Q}_{44}}$.

The stiffness matrix of the thick-walled shaft with the kth $\pm\varphi$ angle layers can be obtained by combining Eq.(4) and Eq.(5), we have Eq.(6) below

$$\begin{Bmatrix} \sigma_z \\ \tau_{z\theta} \\ \tau_{r\theta} \end{Bmatrix}_{\pm\varphi} = \begin{bmatrix} C_{11} & C_{12} & 0 \\ C_{12} & C_{22} & 0 \\ 0 & 0 & C_{33} \end{bmatrix}_{\pm\varphi} \begin{Bmatrix} \varepsilon_z \\ \gamma_{z\theta} \\ \gamma_{r\theta} \end{Bmatrix}_{\pm\varphi} \tag{6}$$

where

$$C_{11}=\bar{Q}_{11}+\frac{2\bar{Q}_{12}\bar{Q}_{13}\bar{Q}_{23}-\bar{Q}_{12}\bar{Q}_{12}\bar{Q}_{33}-\bar{Q}_{13}\bar{Q}_{13}\bar{Q}_{22}}{\bar{Q}_{22}\bar{Q}_{33}-\bar{Q}_{23}\bar{Q}_{23}};$$

$$C_{12}=\bar{Q}_{16}+\frac{\bar{Q}_{12}\bar{Q}_{23}\bar{Q}_{36}-\bar{Q}_{12}\bar{Q}_{26}\bar{Q}_{33}+\bar{Q}_{13}\bar{Q}_{23}\bar{Q}_{26}-\bar{Q}_{13}\bar{Q}_{22}\bar{Q}_{36}}{\bar{Q}_{22}\bar{Q}_{33}-\bar{Q}_{23}\bar{Q}_{23}};$$

$$C_{22}=\bar{Q}_{66}+\frac{2\bar{Q}_{23}\bar{Q}_{26}\bar{Q}_{36}-\bar{Q}_{26}\bar{Q}_{26}\bar{Q}_{33}-\bar{Q}_{36}\bar{Q}_{36}\bar{Q}_{22}}{\bar{Q}_{22}\bar{Q}_{33}-\bar{Q}_{23}\bar{Q}_{23}};$$

$$C_{33}=\bar{Q}_{55}-\frac{\bar{Q}_{45}\bar{Q}_{45}}{\bar{Q}_{44}}.$$

The above equation eliminates some elements because the smallest mechanical unit contains a positive and negative cross-laminations. Therefore, the above equations can be simplified as

$$C_{11}=\bar{Q}_{11}+\frac{2\bar{Q}_{12}\bar{Q}_{13}\bar{Q}_{23}-\bar{Q}_{12}\bar{Q}_{12}\bar{Q}_{33}-\bar{Q}_{13}\bar{Q}_{13}\bar{Q}_{22}}{\bar{Q}_{22}\bar{Q}_{33}-\bar{Q}_{23}\bar{Q}_{23}};$$

$C_{12}=0$; $C_{22}=\bar{Q}_{66}$; $C_{33}=\bar{Q}_{55}$.

Thick-walled shafts satisfy the equation for bending moment balance

$$M_x=\int_A \sigma_z y \mathrm{d}_A \tag{7}$$

where M_x is the bending moment in the x-axis, A

the axial cross-section area of MFRP shaft, d_A a stress unit, y the distance from the stress unit to the axis, and σ_z the stress in the z-axis direction.

Converting a direct coordinate system into a column coordinate system

$$\begin{cases} y = r\sin\theta \\ d_A = r\mathrm{d}\theta \times \mathrm{d}r \end{cases} \tag{8}$$

Substituting Eqs.(7, 8) into Eq.(6) yields

$$\int_0^{2\pi}\int_{r_i}^{r_o} C_{11}\varepsilon_z r^2 \sin\theta \mathrm{d}r\mathrm{d}\theta = M_x \tag{9}$$

$$\varepsilon_z = \frac{-r\sin\theta}{b} \tag{10}$$

where ε_z is the strain in the z-axis direction and b the curvature radius of the bending deformation layer.

Based on the classical layer-wise theory[20], the integral of each layer of the moment balance equation can be expressed as

$$\begin{aligned} &\int_0^{2\pi}\int_{r_i}^{r_o} C_{11}\varepsilon_z r^2 \sin\theta \mathrm{d}r\mathrm{d}\theta = \\ &\quad \int_0^{2\pi}\sum_{k=1}^{N}\frac{1}{b}\int_0^{2\pi}\int_{r_i^k}^{r_o^k} C_{11}^k r^3 \sin^2\theta \, \mathrm{d}r\mathrm{d}\theta = M_x \end{aligned} \tag{11}$$

where

$$\int_0^{2\pi}\int_{r_i^k}^{r_o^k} C_{11}^k r^3 \sin^2\theta \, \mathrm{d}r\mathrm{d}\theta = C_{11}^k \pi \frac{(r_o^k)^4 - (r_i^k)^4}{4}$$

Ultimately, the bending moment balance equation can be obtained as

$$M_x = \sum_{k=1}^{N}\frac{1}{b} C_{11}^k \pi \frac{(r_o^k)^4 - (r_i^k)^4}{4} \tag{12}$$

So the equivalent bending stiffness (EI) of the MFRP shaft can be obtained as

$$EI = \sum_{k=1}^{N} C_{11}^k \pi \frac{(r_o^k)^4 - (r_i^k)^4}{4} \tag{13}$$

where $C_{11}^k = \bar{Q}_{11}^k + \dfrac{2\bar{Q}_{12}^k\bar{Q}_{13}^k\bar{Q}_{23}^k - \bar{Q}_{11}^k\bar{Q}_{33}^k - \bar{Q}_{13}^k\bar{Q}_{22}^k}{\bar{Q}_{22}^k\bar{Q}_{33}^k - (\bar{Q}_{23}^k)^2}$; $\bar{Q}_{12}^k = m^2n^2(Q_{11} + Q_{22} - 4Q_{66})(m^4 + n^4)Q_{12}$; $\bar{Q}_{13}^k = m^2Q_{13} + n^2Q_{23}$; $\bar{Q}_{23}^k = n^2Q_{13} + m^2Q_{23}$; $\bar{Q}_{22}^k = n^4Q_{11} + 2m^2n^2(Q_{12} + 2Q_{66}) + m^4Q_{22}$; $\bar{Q}_{33}^k = Q_{33}$.

The lay-up scheme is expressed in matrix form: $[X_i, Y_j]_t$, where X_i and Y_j are the angles of the inner and outer layers, respectively; t is the stacked approaches, which means repeating internal layers when t is 2. When t is s, it represents the way of symmetric stacking.

Fig.1 shows the structure and loading types of MFRP shaft, where Fig.1(b) is a schematic diagram of the laminated structure concerning the section of Fig.1(a) and Fig.1(c) shows different loading types of MFRP shaft. As can be seen in Fig.1, o is the axis of the MFRP shaft, direction 1 the direction of the fiber, direction 2 the direction perpendicular to the fiber, direction 3 the direction of the composite material layers thickness, φ the fiber orientation angle, L the length of MFRP shaft, R the radius of MFRP shaft, and h the thickness of MFRP shaft. r_o^k and r_i^k are the outer and inner radius of kth layer, respectively. Fig.2 is a schematic diagram of the part stacking structure of MFRP shaft.

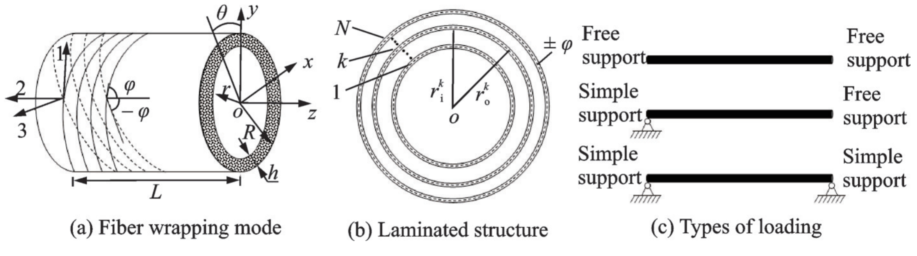

(a) Fiber wrapping mode (b) Laminated structure (c) Types of loading

Fig.1 Diagram of structure and loading types of MFRP shaft

(a) Separated stacking (b) Repeated stacking (c) Symmetric stacking

Fig.2 Schematic diagram of the part of stacking structure of MFRP shaft

1.2 Natural frequency calculation equation of MFRP shaft

1.2.1 Empirical calculation equation of natural frequency

The MFRP shaft is regarded as a beam structure with equal section, and the natural frequency of MFRP shaft in the free state can be calculated according to the empirical calculation equation in Ref.[21], as shown in Eq.(14).

$$f=\frac{11.2}{\pi L^2}\sqrt{\frac{EI}{\rho A}} \tag{14}$$

where EI is the equivalent bending stiffness of MFRP shaft and ρ the density of composite material.

1.2.2 Natural frequency calculation equation based on the transfer matrix method

The MFRP shaft is divided into the disk and axis elements. Transfer matrix theory[22] is used to transfer the parameters from the beginning to the end, and the specific transfer mode is given as follows: The ith node represents the ith axis segment so that the state variable at the right end of the ith unit can be represented by the state at the right end of the $(i+1)$th unit.

Applying Newton's second law to the ith mass-disk, the state of the ith mass-disk can be obtained

$$\begin{cases} y_i^{\mathrm{R}} = y_i^{\mathrm{L}} = y_i \\ \alpha_i^{\mathrm{R}} = \alpha_i^{\mathrm{L}} = \alpha_i \\ M_i^{\mathrm{R}} = M_i^{\mathrm{L}} - (I_d - I_p)_i \omega^2 \alpha_i \\ S_i^{\mathrm{R}} = S_i^{\mathrm{L}} - m_i y_i'' - K_i y_i \end{cases} \tag{15}$$

where R refers to the right end, L the left end, y_i the radial displacement, α_i the deflection angle, M_i the bending moment of cross-section, S_i the shear force, m_i the mass of mass-disk, K_i the supporting stiffness which acts on the mass-disk ($K_i=0\ \mathrm{N\cdot m^2}$), ω the natural frequency of the shaft, I_p the polar moment of inertia of the shaft, and I_d the moment of inertia of the diameter of the shaft.

Convert Eq.(15) into matrix form, and then obtain the point transfer matrix of two ends, as shown in Eq.(16).

$$\begin{pmatrix} y \\ \alpha \\ M \\ S \end{pmatrix}_i^{\mathrm{R}} = \begin{bmatrix} 1 & 0 & 0 & 0 \\ 0 & 1 & 0 & 0 \\ 0 & (I_p - I_d)_i \omega^2 & 1 & 0 \\ \omega^2 m - K_i & 0 & 0 & 1 \end{bmatrix} \begin{pmatrix} y \\ \alpha \\ M \\ S \end{pmatrix}_i^{\mathrm{L}} \tag{16}$$

Based on the bending and deformation theory of beam, the state between two ends can be described as

$$\begin{cases} y_{i+1} = y_i + \alpha_i l_i + \dfrac{M_{i+1}^{\mathrm{L}} l_i^2}{2E_i I_i} - S_{i+1}^{\mathrm{L}} \dfrac{l_i^3}{6E_i I_i}(1-u) \\ \alpha_{i+1} = \alpha_i + M_{i+1}^{\mathrm{L}} \dfrac{l_i}{E_i I_i} - \alpha_{i+1}^{\mathrm{L}} \dfrac{l_i^2}{2E_i I_i} \\ M_{i+1}^{\mathrm{L}} = M_i^{\mathrm{R}} + S_i^{\mathrm{R}} l_i \\ S_{i+1}^{\mathrm{L}} = S_i^{\mathrm{R}} \end{cases} \tag{17}$$

where l is the length of the shaft section and u the shear coefficient ($u=0$).

Convert Eq.(17) into matrix form, and then obtain the field transfer matrix, as shown in Eq.(18).

$$\begin{pmatrix} y \\ \alpha \\ M \\ S \end{pmatrix}_{i+1}^{\mathrm{L}} = \begin{bmatrix} 1 & l & \dfrac{l^2}{2EI} & \dfrac{l^3}{6EI}(1-u) \\ 0 & 1 & \dfrac{l}{EI} & \dfrac{l^2}{2EI} \\ 0 & 0 & 1 & l \\ 0 & 0 & 0 & 1 \end{bmatrix} \begin{pmatrix} y \\ \alpha \\ M \\ S \end{pmatrix}_i^{\mathrm{R}} \tag{18}$$

Substitute Eq.(18) into Eq.(16) to obtain the disk-axis transfer matrix, as shown in Eq.(19).

$$\begin{pmatrix} y \\ \alpha \\ M \\ S \end{pmatrix}_{i+1}^{\mathrm{L}} = \begin{bmatrix} 1+\dfrac{l^3}{6EI}(1-u)(m_i\omega^2 - K_i) & l+\dfrac{l^2}{2EI}(I_p - I_d)\omega^2 & \dfrac{l^2}{2EI} & \dfrac{l^3}{6EI}(1-u) \\ \dfrac{l^2}{2EI}(m_i\omega^2 - K_i) & 1+\dfrac{l}{EI}(I_p - I_d)\omega^2 & \dfrac{l}{EI} & \dfrac{l^2}{2EI} \\ l(m_i\omega^2 - K_i) & (I_p - I_d)\omega^2 & 1 & l \\ (m_i\omega^2 - K_i) & 0 & 0 & 1 \end{bmatrix} \begin{pmatrix} y \\ \alpha \\ M \\ S \end{pmatrix}_i^{\mathrm{R}} \tag{19}$$

Terminal state parameters can be expressed as

$$(y,\alpha,M,S)_{N+1}^{\mathrm{T}}=\prod_{i}^{N}T_i(y,\alpha,M,S)_1^{\mathrm{T}} \tag{20}$$

For the MFRP shaft with free/free support, its boundary conditions at both ends are

$$M_1=0,\ S_1=0;\ M_N=0,\ S_N=0 \tag{21}$$

Substituting Eq.(21) into Eq.(20) yields

$$\begin{bmatrix} a_{31} & a_{32} \\ a_{41} & a_{42} \end{bmatrix}_N \begin{pmatrix} y \\ \alpha \end{pmatrix}=\begin{pmatrix} 0 \\ 0 \end{pmatrix} \tag{22}$$

For the MFRP shaft with simple/free supported state, its boundary conditions at both ends are

$$M_1=0,\ S_1=0;\ Y_N=0,\ M_N=0 \tag{23}$$

Substituting Eq.(23) into Eq.(24) yields

$$\begin{bmatrix} a_{11} & a_{12} \\ a_{31} & a_{32} \end{bmatrix}_N \begin{pmatrix} y \\ \alpha \end{pmatrix}=\begin{pmatrix} 0 \\ 0 \end{pmatrix} \tag{24}$$

Boundary conditions for simple supported cases at both ends are

$$Y_1=0,\ M_1=0;\ Y_N=0,\ M_N=0 \tag{25}$$

Substituting Eq.(25) into Eq.(24) yields

$$\begin{bmatrix} a_{12} & a_{14} \\ a_{32} & a_{34} \end{bmatrix}_N \begin{pmatrix} \alpha \\ S \end{pmatrix}=\begin{pmatrix} 0 \\ 0 \end{pmatrix} \tag{26}$$

By solving the non-zero solutions of Eqs.(22, 24, 26), the natural frequency of MFRP shaft can be obtained under different boundary conditions (free/free support, simple/free support, simple/simple support).

2 Numerical Calculation and Model Validation

To verify the correctness of the equivalent bending stiffness theory of the three-dimensional analytical model established in this paper, the calculated results are compared with the experimental results in Ref.[19], and the comparison results are shown in Table 1. At the same time, in order to verify the correctness of the natural frequency of the MFRP shaft obtained by the transfer matrix theoretical model established in this paper, MFRP shaft with an outer diameter (D= 0.44 m) and length (L= 2.5 m) is taken as the research object. The calculation results obtained by transfer matrix theory are compared with classical empirical calculation. The comparison results are shown in Table 2.

Table 1 Comparison of calculation results with experimental results in Ref.[19]

Combination	Ref.[19] / (N•m^2)	The proposed/ (N•m^2)	Error/%
$[(\pm 45°)_4,\ \pm 5°]_2$	1 180	1 110	5.9
$[\pm 45°,\ (\pm 5°)_4]_2$	2 933	2 930	0.1
$[(\pm 5°)_4,\ \pm 45°]_2$	2 666	2 770	3.9

Table 2 Comparison of calculation results with classical empirical calculation

EI / (N•m^2)	Natural frequency of empirical equation/Hz	Natural frequency of transfer matrix method /Hz	Error/%
9.29e7	401.00	398.79	0.55
1.98e7	185.13	184.10	0.56
9.99e6	131.50	130.77	0.56

As shown in Table 1, the theoretical calculation results of equivalent bending stiffness by the three-dimensional analytical model in this paper are very close to the experimental results in Ref.[19], which are controlled within 6%. Thus, it can be considered that the three-dimensional analytical model established in this paper has high accuracy. Moreover, as shown in Table 2, the calculation deviation of MFRP shaft natural frequency between the empirical equation and transfer matrix method is less than 0.6%, so it can also be considered that the transfer matrix method has high accuracy in solving the natural frequency of MFRP shaft.

3 Calculation and Analysis

The MFRP shaft is composed of T700 carbon fiber and YPH-308 epoxy resin[19], and the specific mechanical parameters are presented in Table 3.

Table 3 Mechanical parameters of MFRP

Young's modulus/GPa			Poisson's ratio			Shear modulus/GPa			Density ρ/(kg•m^{-3})
E_1	E_2	E_3	ν_{12}	ν_{23}	ν_{13}	G_1	G_2	G_3	
150	9	9	0.24	0.28	0.24	5.12	3.34	5.12	1 650

3.1 Influences on equivalent bending stiffness

The effect of different layer angles on the equivalent bending stiffness of MFRP shaft with different thickness-radius ratios was studied, as shown in Fig.3. Meanwhile, the control variable method was adopted to study the influence of factors (layer angles, layer proportion, and stacked approaches) on the equivalent bending stiffness of MFRP shaft (D=0.44 m, L=2.5 m) under different thickness-radius ratios (h/R), as shown in Fig.4.

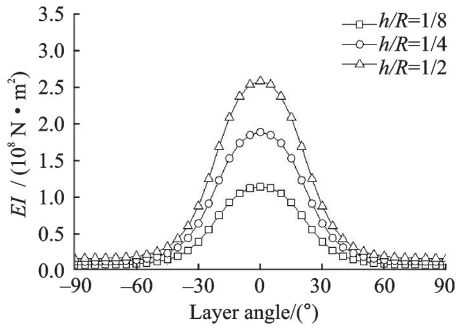

Fig.3 Effect of different layer angles on the equivalent bending stiffness of MFRP shaft with different thickness-radius ratios

As shown in Fig.3, the equivalent bending stiffness of MFRP shaft for different layer angles within ±90° shows a normal distribution, and it can be seen that the smaller layer angles within ±45°, the higher the equivalent bending stiffness of MFRP shaft, while the layer angles beyond ±45° have less influence. In addition, the graph also shows that the equivalent bending stiffness of MFRP shaft comes higher with the increase of thickness-radius ratio, and the effect of thickness-radius ratios on MFRP shaft equivalent bending stiffness is greater when the layer angles are within ±45°, and the smaller the layer angle, the greater the difference in magnitude.

Combined with Fig.4(a) and Fig.4(b), it can be seen that regardless of the stacked approaches, the proportion of small-angle layers is the main influencing factor on MFRP shaft equivalent bending stiffness when the thickness-radius ratio is certain. Specifically, the MFRP shaft equivalent bending stiffness comes higher with increasing the number of small-angle layers. Moreover, the position of the small-angle layers in the inner and outer of the MFRP shaft determines its equivalent bending stiffness, because the MFRP shaft's equivalent bending stiffness is higher when the small-angle layers are located on the outer side. In addition, the equivalent bending stiffness of the MFRP shaft increases integrally with the increase of thickness-radius ratio (h/R).

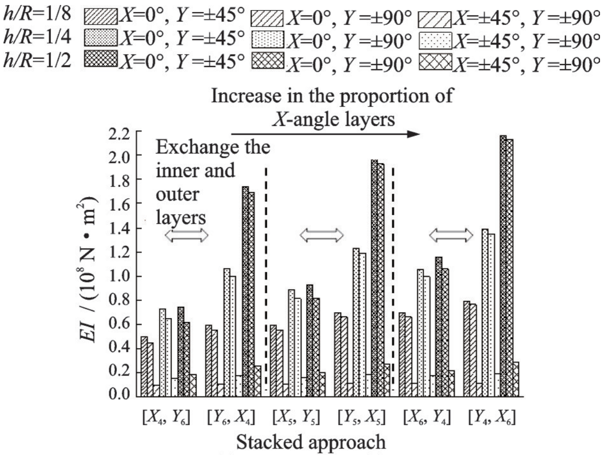

(a) Separated stacking

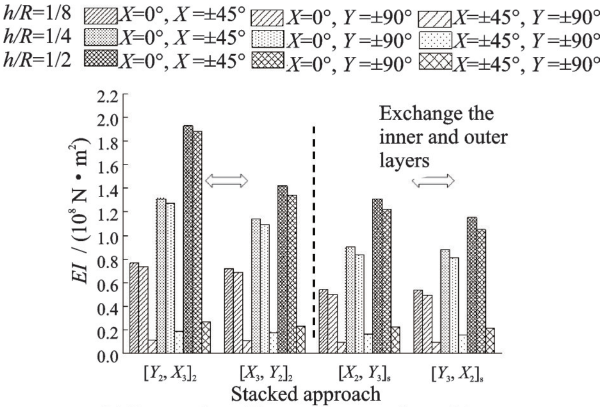

(b) Repeated stacking and symmetric stacking

Fig.4 Effect of factors on the equivalent bending stiffness of MFRP shaft with different thickness-radius ratios

3.2 Influences on the natural frequency

The effect of factors (layer angles, layer proportion, and stacked approaches) on the natural frequency of MFRP shaft with different thickness-radius ratios are investigated (L/R=10, free/free support), as shown in Fig.5(a). Meanwhile, the effect of factors (layer angles, layer proportion, and stacked approaches) on the MFRP shaft natural frequency with different length-radius ratios are investigated ($h/R=1/2$, free/free support), as shown in Fig.5(b), Fig.6(a) and Fig.6(b).

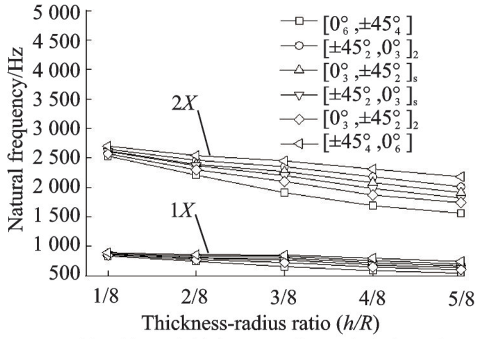

(a) Effect of thickness-radius ratio($L/R=10$)

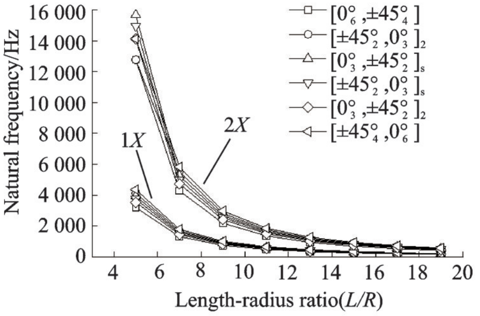

(b) Effect of length-radius ratio($h/R=1/2$)

Fig.5 Influence of factors on the natural frequency of MFRP shaft with different thickness-radius and length-radius ratios

As shown in Fig.5(a), it can be seen that the first-order and the second-order natural frequency of the MFRP shaft decrease with the increase of thickness-radius ratio for a certain proportion of layers laid at each angle, and the difference between the natural frequency of MFRP shaft obtained by each lay-up method is amplified. As shown in Fig.5(b), the difference in the first-order natural frequency of the MFRP shaft obtained by each stacked approach is small after the length-radius ratio reaches 11, while the difference on the second-order natural frequency of the MFRP shaft obtained by each stacked approach is small after the length-radius ratio reaches 15. This means that the length-radius ratio has little effect on the natural frequency of the MFRP shaft after the length-radius ratio is greater than 15. Combining Fig.5(a) and Fig.5(b), it can be seen that the natural frequencies of the MFRP shafts with different layer angles and stacked approaches subsequently decrease with increasing thickness-radius ratio and length-radius ratio.

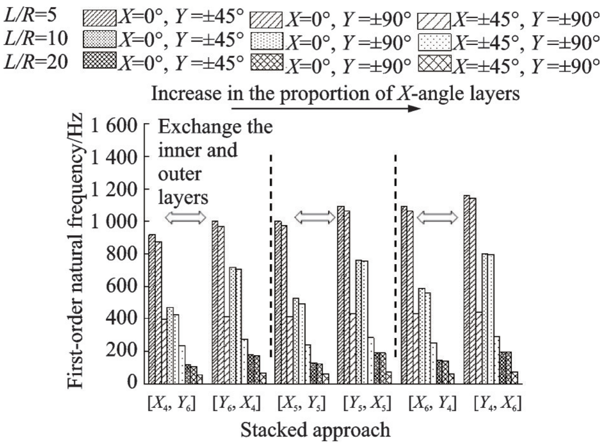

(a) Separated stacking

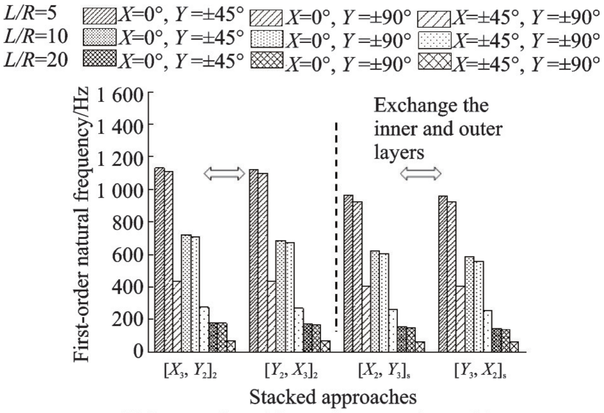

(b) Repeated stacking and symmetric stacking

Fig.6 Influence of factors on the MFRP shaft natural frequency with different length-radius ratios

Combining Fig.6(a) and Fig.6(b), it can also be seen that the proportion of small-angle layers is the decisive factor for the MFRP shaft natural frequency when the length-diameter ratio is certain. Specifically, the natural frequency of the MFRP shaft comes higher when increasing the number of small-angle layers. For either stacked approach, the position of the small-angle layers on the inner and outer of the MFRP shaft determines the natural frequency of the MFRP shaft, because the natural frequency of the MFRP shaft is higher when the small-angle layers are located on the outer side. The reason for this phenomenon is that the radius of the small-angle layers is different when their location varies. Their cross-sectional area is larger when the small-angle layers are located on the outer side of the MFRP shaft, which is in line with the above-mentioned conclusion that the proportion of small-angle layers plays a decisive role in the natural frequency of the MFRP shaft.

3.3 Influences on different boundary conditions

The first-order natural frequency of the MFRP shaft ($h/R=1/2$, $D=0.44$ m, $L=2.5$ m) with different layer angles, layer proportion, and stacked approaches was investigated for simple/free support and simple/simple support, respectively, which compared with the first-order natural frequency of the same size metal shaft (See Fig.7). The mode shapes of the shaft under different boundary conditions are shown in Fig.8.

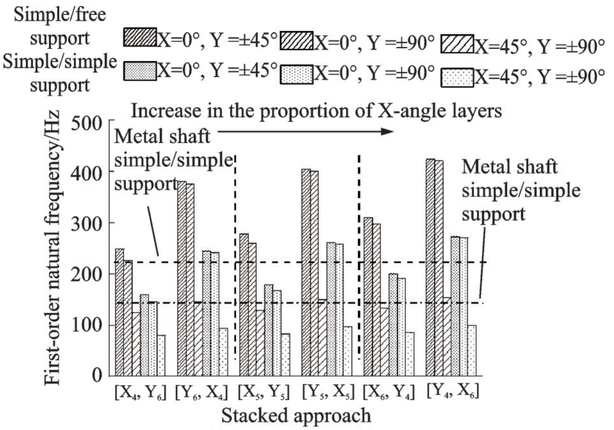

(a) Separated stacking

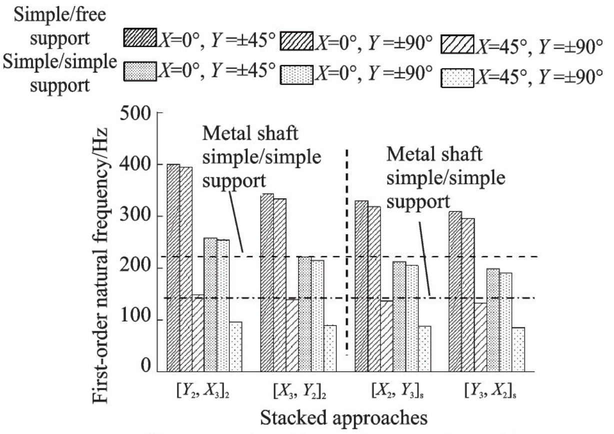

(b) Repeated stacking and symmetric stacking

Fig.7 Comparison of the natural frequency of MFRP shaft and metal shaft under different boundary conditions

As shown in Fig.7, for all boundary conditions, it can be seen that the proportion of small-angle layers is the decisive factor for the natural frequency of MFRP shaft when the length-diameter ratio is certain. Specifically, the natural frequency of MFRP shaft comes higher with the increase of small-angle layers. For either stacked approach, the position of the small-angle layers on the inner and outer of the MFRP shaft determines the magnitude of the natural frequency of the MFRP shaft, the natural frequency of the MFRP shaft is greater when the small-angle layers are located on the outer side. The natural frequency of the MFRP shaft is greater in the simple/free boundary condition than in the simple/simple supported boundary condition for either stacked approach. Under the same boundary conditions, the natural frequency of the MFRP shaft with the angle layers ombination of ±45° and ±90° is less than the metal shaft, while the remaining combinations of angle layers are greater than the metal shaft. The above phenomena suggest that a certain proportion of small-angle layers (small-angle layers within ±45°) needs to be met to obtain a MFRP shaft design that is superior to the natural frequency of the metal shaft section.

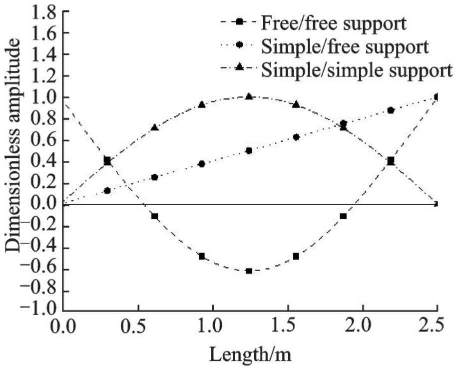

Fig.8 Mode shapes of the shaft under different boundary conditions

As shown in Fig.8, the mode shape of MFRP shaft is the same as metal shaft under the same boundary conditions. Because mode shape reflects the inherent properties of the system, and it is the normalized deformation under its natural frequency. Thus the mode shape will be determined once the boundary condition is given. However, in forced vibration calculation, the displacement response varies due to the existence of damping in MFRP shaft.

In summary, the dynamics of MFRP shaft are mainly influenced by its stacking parameters. The variation of MFRP shaft natural frequency under different boundary conditions is the same as metal shaft.

4 Conclusions

Based on the coupling model of three-dimensional equivalent bending stiffness theory and transfer matrix method, this paper studies the influence of layer angles, layer proportion, and stacked approaches on the natural frequency of MFRP shaft under different thickness-radius ratios, length-radius ratios, and different boundary conditions. Several conclusions are as follows:

(1) The coupling model of three-dimensional equivalent bending stiffness theory and transfer matrix method is applicable to the dynamics characteristics of MFRP shaft. And its prediction accuracy is high.

(2) The proportion of small-angle layers is a decisive factor in the natural frequency of the MFRP shaft.

(3) For either stacked approach, the natural frequency of the MFRP shaft decreases with increasing thickness-radius ratio and length-radius ratio for different layer angles and layer proportion.

(4) The natural frequency of MFRP shaft with the angle layers combination of ±45° and ±90° is less than the metal shaft no matter in simple/free boundary condition or simple/simple supported boundary condition, while the remaining combinations of angle layers are greater than the metal shaft.

References

[1] CHEN Gang, WANG Xiaopei, SONG Jun, et al. Structural design and test verification of composite wing for high load and large sweepback UAVs[J]. Journal of Nanjing University of Aeronautics & Astronautics, 2021, 53(4): 613-619. (in Chinese)

[2] ZHONG H F, HE Q X, ZU L. Optimization of fiber winding composite drive shaft based on ANSYS[J]. FRP/Composite, 2015(3): 20-25. (in Chinese)

[3] CHEN W M, WANG C Z, ZHOU T Y, et al. High performance T800 carbon fiber composite resin matrix[J]. Acta Materiae Compositae Sinica, 2006(4): 29-35.(in chinese)

[4] ZHENG Yuqiao, LIU Zheyan, MA Huidong, et al. Optimization of composite wind turbine blade based on modal sensitivity[J]. Transactions of Nanjing University of Aeronautics and Astronautics, 2021, 38(1): 153-163.

[5] JAMES P, SRIKANTH D V, KUMAR T S, et al. Design and analysis of automotive plastic propeller shaft using fea[J]. Materials Today Proceedings, 2016, 3(10): 3673-3679.

[6] BADIE M A, MAHDI E, HAMOUDA A. An investigation into hybrid carbon/glass fiber reinforced epoxy plastic automotive drive shaft[J]. Materials & Design, 2011, 32(3): 1485-1500.

[7] MENSHYKOVA M, GUZ I A. Stress analysis of layered thick-walled plastic pipes subjected to bending loading[J]. International Journal of Mechanical Sciences, 2014, 88: 289-299.

[8] SUN Z Y, XIAO J, YU X D, et al. Vibration characteristics of carbon-fiber reinforced plastic drive shafts fabricated using filament winding technology[J]. Plastic Structures, 2019, 241: 111725.

[9] GUBRAN H, GUPTA K. The effect of stacking sequence and coupling mechanisms on the natural frequencies of composite shafts[J]. Journal of Sound and Vibration, 2005, 282: 231-248.

[10] GUBRAN H. Dynamic stress analysis in fibre-reinforced composite shafts[D]. Delhi, India: Indian Institute of Technology (IIT), 2000.

[11] SINO R, BARANGER T N, CHATELET E, et al. Dynamic analysis of a rotating composite shaft[J]. Composites Science & Technology, 2008, 68(2): 337-345.

[12] SEVKAT E. Finite element analysis of functionally hybridized carbon/glass composite shafts[J]. Journal of Reinforced Plastics & Composites, 2014, 33(13): 1226-1236.

[13] SAEED K, ALIREZA S, SIRUS J. Designing and optimizing of composite and hybrid drive shafts based on the bees algorithm[J]. Journal of Mechanical Science and Technology, 2016, 30(4): 1755-1761.

[14] MONTAGNIER O, HOCHARD C. Optimisation of hybrid high-modulus/high-strength carbon fibre reinforced plastic composite drive shafts[J]. Materials & Design, 2013, 46(4): 88-100.

[15] KHOSHRAVAN M R, PAYKANI A. Design of a composite drive shaft and its coupling for automotive application[J]. Journal of Applied Research and Technology, 2012, 10(6): 826-834.

[16] DING G, XIE C, ZHANG J, et al. Modal analysis based on finite element method and experimental validation on carbon fibre plastic drive shaft considering

steel joints[J]. Materials Research Innovations, 2016, 19(5): 748-753.

[17] REN Y S, DAI Q Y, ZHANG X Q. Free vibration and stability of rotating composite thin-walled shaft[J]. Journal of Vibration Engineering, 2015, 28(1): 59-66.

[18] DING G P, DAI Z L, ZHU Y, et al. Modal analysis of carbon fiber composite transmission shaft based on transfer matrix method[J]. Machinery Design & Manufacture, 2019(5): 56-59.

[19] YANG M. Modeling and characteristics of carbon fiber composite drive shafting system[D]. Wuhan: Wuhan University of Technology, 2018.

[20] SHADMEHRIF, HADDADPOURH, KOUCHAKZADEH M A. Flexural-torsional behavior of thin-walled plastic beams with closed cross-section[J]. Thin-Walled Structures, 2007, 45(7): 699-705.

[21] DABROWSKI Z, DEUSZKIEWICZ P. Dynamic model of carbon fiber drive shaft[J]. Solid State Phenomena, 2015(236): 39-52.

[22] ZHONG Y E. Rotor dynamics[M]. Shanghai: Tsinghua University Press, 1987.

Authors Mr. **QIAN Haiyu** received the B. S. degree in New Energy Science and Engineering from Yangzhou University in 2019. Since 2019, he has been studying for a master's degree at Jiangsu University of Science and Technology. His research is focused on rotor dynamics.

Dr. **ZHU Junchao** received the B.S. degree in Physics from Jiangsu University of Science and Technology in 2010 and the Ph.D. degree in Transportation Engineering from Wuhan University of Science and Technology in 2019, respectively. He joined in Jiangsu University of Science and Technology in February 2020. His research is focused on rotor dynamics and bearing lubrication.

Author contributions Mr. **QIAN Haiyu** complied with the models and wrote the manuscript. Dr. **ZHU Junchao** contributed to the background of the study and designed the study. Prof. **WEN Huabing** revised and modified the manuscript. Mr. **HE Congshuai** translated and proofread the text. All authors commented on the manuscript draft and approved the submission.

Competing interests The authors declare no competing interests.

(Production Editor: XU Chengting)

多层纤维增强复合材料轴的动力学特性分析

钱海俣,朱军超,温华兵,何从帅

(江苏科技大学能源与动力学院,镇江 212100,中国)

摘要:为了研究多层纤维增强复合材料(Multilayer fiber reinforced plastic,MFRP)轴的动态特性,建立了三维等效弯曲刚度理论和传递矩阵法的耦合模型,研究了厚径比、长径比、铺层角度、铺层占比和堆叠方法对MFRP轴动态特性的影响。结果表明:该耦合模型对MFRP轴动态性能预测具有较高的精度。小角铺层占比是MFRP轴固有频率大小的决定性因素。随着厚径比、长径比的增大,MFRP轴的固有频率减小。无论在简支/自由边界条件还是简支/简支边界条件下,±45°和±90°铺层组合的MFRP轴的固有频率均小于金属轴。

关键词:多层纤维增强复合材料轴;动力学特性;固有频率